Communication

Additive Manufacturing of High Refractive Index, Nano-architected Titanium Dioxide for 3D Dielectric Photonic Crystals

Andrey Vyatskikh, Ryan C. Ng, Bryce Edwards, Ryan M. Briggs, and Julia R Greer

Nano Lett., **Just Accepted Manuscript** • Publication Date (Web): 27 Apr 2020

Additive Manufacturing of High Refractive Index, Nano-architected Titanium Dioxide for 3D Dielectric Photonic Crystals

Andrey Vyatskikh[1], Ryan C. Ng[2], Bryce Edwards[1], Ryan M. Briggs[3], and Julia R. Greer[1,*]

[1]Division of Engineering and Applied Science, California Institute of Technology, 1200 E. California Blvd., Pasadena, CA 91125, USA

[2]Division of Chemistry and Chemical Engineering, California Institute of Technology, 1200 E. California Blvd., Pasadena, CA 91125, USA

[3]Jet Propulsion Laboratory, California Institute of Technology, 4800 Oak Grove Dr, Pasadena, CA 91109

*Correspondence to: jrgreer@caltech.edu

Abstract

Additive manufacturing at small scales enables advances in micro- and nano-electromechanical systems, micro-optics, and medical devices. Materials that lend themselves to AM at the nano-scale, especially for optical applications, are limited. State-of-the-art AM processes for high refractive index materials typically suffer from high porosity, poor repeatability, and require complex experimental procedures.

We developed an AM process to fabricate complex 3D architectures out of fully dense titanium dioxide (TiO_2) with a refractive index of 2.3 and nano-sized critical dimensions. Transmission Electron Microscopy (TEM) analysis proves this material to be rutile phase of nanocrystalline TiO_2, with an average grain size of 110 nm and <1% porosity. Proof-of-concept woodpile architectures with 300-600 nm beam dimensions exhibit a full photonic bandgap centered at 1.8-2.9 μm, revealed by Fourier-transform Infrared Spectroscopy (FTIR) and supported by Plane Wave Expansion simulations. The developed AM process enables advances in 3D MEMS, micro-optics, and prototyping of 3D dielectric PhCs.

Keywords: additive manufacturing, titanium dioxide, hybrid organic-inorganic material, two-photon lithography, high refractive index, photonic crystals

TOC graphic

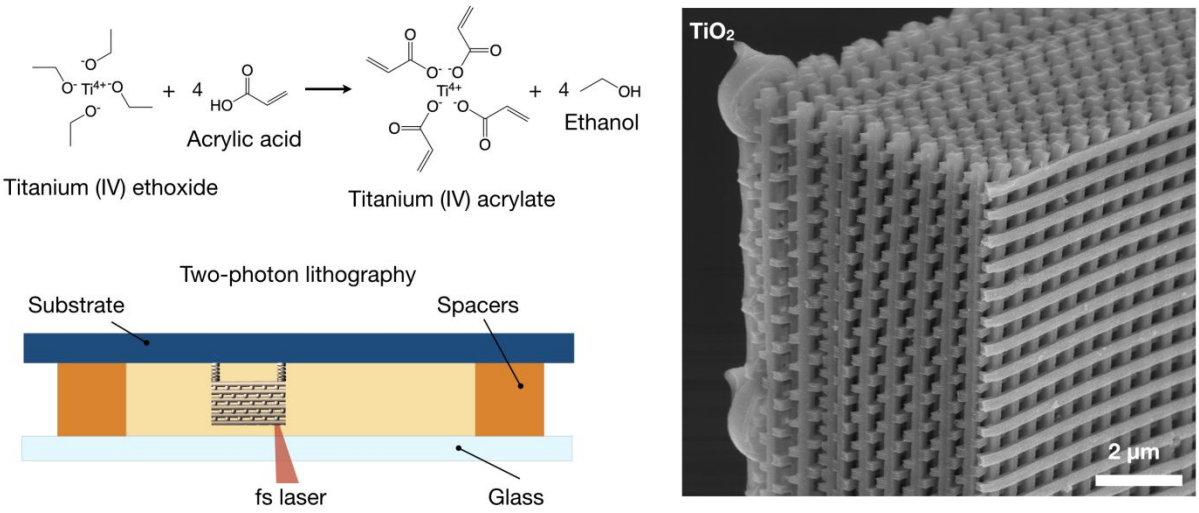

Introduction

Additive manufacturing (AM) represents a set of processes for layer-by-layer fabrication of 3D parts out of polymers, metals, and ceramics[1–3]. At the micro- and nano-scales, AM is poised to become the enabling technology for efficient 3D MEMS, micro-battery electrodes, electrically small antennae, and micro-optical components[4–7]. Facilitating these technologies requires a fabrication process to create a variety of functional materials in 3D, however the material choice for AM at the nano- and micro-scale is limited. This limitation is especially pronounced when particular material properties, including piezoelectric, magnetic, or optical, are required for the final application[8–10].

A conspicuous example is a lack of AM processes for high refractive index (*n)*, low absorption materials with nano-sized dimensions[11], which are typically required for micro-optics and device applications. Polymer materials that can be shaped using direct laser writing (DLW) methods, such as two-photon lithography (TPL), are limited to refractive indices below 1.8[12]. Hybrid materials for TPL that consist of inorganic silica-type networks

with embedded heteroatoms, including Zr, Zn, and Ge, have been demonstrated, but their refractive indices were below 1.6[13–16]. Direct Laser Writing (DLW) of As_2S_3 chalcogenide glasses with *n* between 2.45 and 2.53 in the infrared has been demonstrated by taking advantage of their photo-induced metastability[9], but the high index mismatch between the lens and the printed material complicated the feature size control. Metal oxides with refractive indices *n*~1.9 have been nano-architected using DLW of aqueous metal-containing photopolymers followed by calcination, but the low metal ion loading in these resins led to linear shrinkage of up to 87%, which made it challenging to preserve complex 3D geometry[8,17]. TPL of organic-inorganic resists combined with post-lithography thermal treatment has shown promise to create 3D nanolattices of metals and ceramics, but the residual porosity of up to 20% within the beams reduces the effective refractive index[18,19]. An AM process that can repeatably and accurately produce 3D architectures with sub-micron geometrical features out of high refractive index, low absorption material is yet to be developed and would realize multiple micro-optical devices and three-dimensional (3D) dielectric photonic crystals (PhCs)[10].

3D dielectric PhCs have been a focus of extensive research for their unique ability to tailor and manipulate light[20,21]. 3D PhCs with a full photonic bandgap [22,23], 3D chiral PhCs that control light polarization[24], and all-angle negative refractive (AANR) index materials[25] have been demonstrated. Each of these devices is enabled by satisfying stringent optical material requirements and dimensional control. For example, obtaining a full photonic bandgap in woodpile architectures requires constituent materials with a refractive index $n \gtrsim 1.9$[26], and attaining AANR requires an effective index of $n \geq 2.49$[27], with individual features smaller than the target wavelength. Creating nano-sized three-dimensional architectures out of high refractive index materials, such as silicon (Si), gallium arsenide (GaAs), and titanium dioxide (TiO_2), can only be achieved via sophisticated experimental procedures. Examples include

micromanipulation of individually stacked layers[28] or single- or double-inversion of a polymer templates that often result in features with up to 16% porosity[10,23].

Titanium dioxide (titania, TiO_2) represents a beneficial material choice for 3D dielectric PhCs in the visible and the infrared because of its high refractive index and high transparency[10]. The highest refractive index, between 2.45 and 3.03 for 500-1500 nm wavelengths, is attained in the rutile phase of TiO_2[29]. The processes for AM of titania demonstrated to date suffer from high porosity, low refractive index of the constituent material, and poor repeatability. An ideal AM process for titania would have to repeatably and accurately produce 3D structures with sub-micron features out of fully dense rutile TiO_2. Several previous studies have described AM processes for TiO_2. Direct Ink Writing (DIW) of sol-gel inks followed by calcination has been shown to produce TiO_2 features with sub-micron dimensions that are ~10% porous and contained about a half of a lower-index anatase phase, which lowered their effective refractive index by at least 10%[30]. Femtosecond laser processing of liquid TiO_2 precursors has been used to selectively introduce insoluble regions into the patterned material by breaking chemical bonds, but the poor adhesion between the sample and the substrate led to the loss of heat-treated 3D structures[18]. Laser-induced decomposition of sol-gel precursors enabled 2D patterning of TiO_2/carbon composites with typical feature widths of 3 μm for crystalline TiO_2 and has not been extended to three dimensions[31]. Using hybrid organic-inorganic materials in AM has been demonstrated for a stereolithography (SLA)-based patterning to create architected titania with 150 μm feature sizes. This process could not be extended to sub-micron features due to the resolution limit of SLA[32]. We previously showed feasibility of AM of 3D nano-architected titania using two-photon lithography; this approach did not achieve precise dimensional control required for the emergence of a full photonic bandgap[33].

We demonstrate an AM process capable of repeatably and accurately producing 3D nano-architected titanium dioxide, with critical feature dimensions between 150 and 600 nm and <1% porosity. We synthesize a hybrid organic-inorganic precursor to formulate a pre-ceramic TiO_2 resist. We use two-photon lithography to pattern the designed 3D shapes and pyrolyze them at 750-900°C in air. This process shrinks the dimensions of originally patterned 3D nano-architectures by 60% to produce fully dense nanocrystalline TiO_2 replicas. As a proof of concept, we created 3D dielectric PhCs using this process by fabricating rutile TiO_2 patterned into woodpile face-centered tetragonal (FCT) architectures with beam dimensions of 300-600 nm and lateral periods of 0.8-1.5 μm. We use Plane Wave Expansion (PWE) simulations and Fourier Transform Infrared Spectroscopy (FTIR) to demonstrate the full photonic bandgaps centered at 1.8-2.9 μm. AM process for fabricating 3D nano-architected fully dense TiO_2 will be crucial for rapid prototyping and manufacturing of 3D PhCs and micro-optical devices.

Results

Process for AM of 3D nano-architected titania

To prepare titania pre-ceramic photopolymer, we first used a ligand exchange reaction between titanium (IV) ethoxide and acrylic acid in 1:4 molar ratio to synthesize titanium (IV) acrylate (Fig. 1A). The reaction was conducted in a glovebox to minimize exposure to oxygen and water. The resulting hybrid organic-inorganic TiO_2 precursor can be embedded in a polymer network during free-radical polymerization. When combined with an acrylic monomer, pentaerythritol triacrylate, the solution becomes clear and orange. A two-photon photoinitiator, 7-diethylamino-3-thenoylcoumarin (DETC), was then dissolved in dichloromethane and added to the solution (see Methods); the resulting liquid photoresist was drop cast onto a silicon substrate and 3D printed in a TPL system (Photonic Professional GT, Nanoscribe GmbH). Architected samples were designed to rest on top of a 2D lattice layer supported by a spring-and-pillars array that decoupled the architecture from the substrate

during pyrolysis and minimized its distortion during shrinkage[19,33] (Figs. 1B, C). Non-polymerized resist was washed away, and free-standing architectures were pyrolyzed in air at 900°C for 1 hr (see Methods) to create replicas of the original structures, with a concomitant ~60% reduction in dimensions, made entirely out of titanium dioxide (Fig. 1D).

Feature dimensions

To ensure high accuracy of geometric dimensions in devices fabricated using this AM process, we carefully studied the influence of process parameters on the size of individual features. Previous studies[34–36] reported strong non-linear dependence of the dimensions of the polymerized material, or voxel, on the laser power (LP) and the exposure time (ET) in two-photon lithography, which is unique for each photopolymer. We used ascending scan experiments[34] to evaluate the voxel width and height for this hybrid photoresist for LP between 12.5 and 20 mW and ET between 0.5 and 10 ms. Fig. S1 shows that for ET between 1 ms and 10 ms at 20 mW, the voxel width varied from 440 to 560 nm, its height changed from 1.6 to 3.2 μm, and the voxel aspect ratio varied from 3.8 to 5.3.

To predict and reliably control the feature size for 3D photonic crystal fabrication, we adopted a model by Serbin et al.[35] that links the voxel dimensions in a two-photon lithography process to the laser exposure parameters (see Supporting Information). Voxel height L (Equation (1)) and voxel width d (Equation (2)) can be expressed as

$$L = 2z_R\sqrt{\sqrt{\alpha t P^2} - 1}, \quad (1)$$

$$d = w_0\sqrt{\log\left[\alpha t P^2\right]}, \quad (2)$$

where z_R is the Rayleigh distance of the objective [m], w_0 is the laser beam waist [m], and $\alpha t P^2$ is a non-dimensional parameter, where t is the exposure time [s], P is the laser power [W], and α is a constant that depends on the exposure pattern and the photopolymer formulation (see Supporting Information). Figure S1 demonstrates that experimentally

measured voxel dimensions are in good agreement with this model, which provides a quantifiable way to tailor the laser exposure parameters to achieve target feature dimensions.

Accuracy and repeatability of geometric features

We demonstrate the efficiency of this approach by fabricating 3D architectures with tetragonal woodpile geometry that has overall dimensions of 220 x 220 μm, a lateral period x_L of 3.7 μm, an axial factor (defined as the ratio of the axial period x_a to the lateral period x_L) of 1.1, and rectangular beams with 1.3 x 1.5 μm cross-sections. Figure 1(F, G) shows SEM images of a representative woodpile structure after pyrolysis that contains 60 periods in the lateral direction and 9 periods in the axial direction. The beams in this sample had 530 x 600 nm rectangular cross-sections, a lateral period of 1.47 μm, and overall lateral dimensions were 95 x 95 μm. The features appeared to be uniform, and the shrinkage post-pyrolysis appeared to be isotropic.

To quantify the effect of shrinkage on geometrical distortions within the structure, we analyzed the variability of geometric dimensions in axial (Fig. S2) and lateral directions in the woodpile using SEM measurements (Table S1). We found that in the axial direction the lateral period did not vary by more than 5%, with no statistically significant deviations in the average beam width (Fig. S2). In the lateral direction, we analyzed the variability of the lateral period using nested variance analysis[37], which revealed a total variability of 25 nm, or 1.7% of the target dimension, across the entire sample (Table S2). We also found that the contribution of spatial variability of the lateral period was only 13 nm, or less than 1% of the target (Table S2).

Material characterization

To characterize the chemical composition of as-fabricated material, we conducted energy-dispersive X-ray spectroscopy (EDS) on a representative sample with in-plane dimensions of

95 x 95 μm and a lateral period of 1.5 μm (Fig. 2A). SEM EDS maps (Fig. 2B-D) show a uniform distribution of Ti and O throughout the structure with no apparent segregations into titanium- or oxygen-rich phases. EDS spectrum taken from a 20 x 20 μm area in the center of the sample (Fig. 2E) reveal the chemical composition to be 66.8 at% oxygen and 33.2 at% titanium. Silicon substrate was excluded from the composition estimate.

To evaluate the phase composition, Raman spectra were collected from the as-fabricated 3D architectures using a 514 nm laser focused through a 50x microscope objective. Fig. 2F shows a representative Raman spectrum along with the reference spectra collected from rutile and anatase samples (see Methods). The Raman signature revealed peaks at 145 cm^{-1}, 448 cm^{-1}, and 613 cm^{-1} that match the rutile reference spectrum.

We analyzed the atomic-level microstructure of as-fabricated TiO_2 structures using Transmission Electron Microscopy (TEM) and electron diffraction. We prepared a 100 nm-thick cross-section of a sample whose beams had 960 x 150 nm elliptical cross-sections, lateral periodicities of 1090 nm, and a footprint of 70 x 70 μm using Focused Ion Beam (FIB) lift out procedure (Fig. 3A). High-resolution (Fig. 3B) and dark-field (Fig. 3C) TEM images reveal that a typical beam cross-section is >99% dense and is comprised of nanocrystallites with a mean size of 110 nm (see Figs. 3D, S3, and S4). Electron diffraction pattern (Fig. 3B, inset) confirms the crystalline phase of TiO_2 to be rutile.

Optical behavior

We used Plane Wave Expansion (PWE) simulations and Fourier Transform Infrared Spectroscopy (FTIR) measurements to investigate the optical behavior of TiO_2 woodpiles. We chose experimentally-equivalent geometric parameters extracted from images in Fig. 1(F,H) and a refractive index of 2.3, obtained by ellipsometry measurements on as-fabricated films (Fig. S5) for PWE simulations. Figure 4A shows the band diagram with the

corresponding Brillouin zone (inset) calculated for an FCT woodpile architecture with these properties, which exhibits a full photonic bandgap between frequencies of 0.465($2\pi c/x_L$) and 0.474($2\pi c/x_L$) (see Fig. S6), where x_L is the lateral period of the woodpile and c is the speed of light. Woodpiles with x_L of 1.47 μm have gap edges at 3.10 and 3.16 μm (Table S2).

To probe the simulation results experimentally, we measured the reflectance and transmittance of the as-fabricated woodpiles using FTIR with a Cassegrain objective with an angle range between 16° and 35.5° within a 30 x 30 μm area at the center of the sample. Previous experimental studies revealed that the position of FTIR reflectance bands is influenced by the stop-band positions that are being probed simultaneously at off-normal light incidences[23]. We calculated the expected stop-band edges from the woodpile band diagram probed along X'-U'-L and X'-W'-K' at experimental off-normal incidence angles to be between 0.418($2\pi c/x_L$) and 0.544($2\pi c/x_L$), which corresponds to the wavelengths of 2.7 to 3.5 μm (Table S2). Fig. 4B contains FTIR spectra that reveals a high reflectance/low transmittance band centered at ~2.9 μm, plotted along with the computed position of a full photonic bandgap (gray rectangle) and the range of stop-band positions for the 16°-35.5° incidence angles (vertical dash lines). The position of the high reflectance band was found to be within 7% from the expected full photonic bandgap.

Varying the TiO_2 precursor loading in the photopolymer enables control over the amount of post-pyrolysis linear shrinkage and of the structural feature sizes, which enables access to multiple wavelengths. We fabricated 3D photonic crystals with reduced lateral periods of 1.12, 1.03, and 0.84 μm by starting with the same pre-ceramic 3D sample and varying the TiO_2 precursor loading by 50-83% (Fig. 4C). These structures were replicas of the titania woodpiles with x_L=1.47 μm shown in Fig. 1F. Figure 4D shows FTIR reflectance spectra for these samples, as well as the computed bandgap positions, that revealed high reflectance

bands centered at 1.8 um, 2.2 um, and 2.4 um, which are within 0.3%, 4.8%, and 3.0% of the target full photonic bandgap positions (Table S2).

Discussion

We developed an AM process to produce three-dimensional networks of fully dense sub-micron features out of a transparent, high refractive index material that can be used to fabricate 3D dielectric photonic crystals. Compositional and microstructural analysis suggests that as-fabricated material is comprised of fully dense nano-crystalline rutile TiO_2 with minimal carbon content. EDS revealed the chemical composition of 33.2 at% Ti and 66.8 at% O, which corresponds to a 1:2 atomic ratio of Ti to O characteristic of titanium dioxide. It is not possible to accurately determine C content using EDS because of its low sensitivity to light elements and because of inevitable carbon contamination in the SEM chamber[38]. Inclusion of the carbon peak in the EDS spectrum fit did not result in the fit improvement, which further corroborates extremely low at% C. Processes based on laser-driven formation of TiO_2/carbon composites yielded a substantial amount of carbon[31] that can lower the material transparency.

TEM electron diffraction and Raman spectroscopy identified TiO_2 to be in its rutile phase. Raman spectrum taken from a representative architected sample revealed peaks that are in good agreement with first-order vibration modes found in rutile titania[39] (B_{1g} at 145 cm^{-1}, E_g at 448 cm^{-1}, and A_{1g} at 613 cm^{-1}), as well as with characteristic second-order scattering around 240 cm^{-1} (see Fig. 2F). This finding is also consistent with other works that studied phase transformation in sol-gel derived titanium dioxide[30,40]. For example, dry sol-gels of TiO_2 were found to convert from anatase into rutile at 550°C, with full transformation occurring at 800°C [40]. These studies suggest rutile as the predominant expected phase of titania resulting from a heat treatment at 900°C. Previous attempts to develop a titania AM process resulted in partially converted TiO_2 (e.g., rutile/anatase mix of 47 wt%/53 wt% in

ref.[30]) and porous features with 10-16% air content[10,30], which lowered the effective refractive index of individual features.

The ability to predict and reliably control the feature size based on the exposure parameters was critical for fabrication of 3D photonic crystals. Estimating polymerization volume in two-photon lithography generally requires numerical simulations that take into account radical generation and inhibition, oxygen diffusion, local heating, and many other factors[36]. We studied the dependence of the voxel dimensions on the exposure parameters by examining polymerization kinetics inside the voxel volume at millisecond time scales. Mueller et al.[41] experimentally showed that at exposure times between 1 and 10 ms two-photon polymerization is primarily driven by radical generation. Uppal et al. found that the generated radicals remain mostly confined to the voxel volume during the exposure[36]. Mueller et al.[42] has demonstrated that the temperature inside the polymerizing voxel did not increase by more than 5K at 20 mW laser power. These previous studies allowed us to adopt a closed-form solution by Serbin et al. for an isothermal system with no diffusion to predict the voxel dimensions in our system.

FTIR reflectance and transmittance spectra of four woodpile samples (Fig. 4B, D) revealed that the observed high reflectance peaks were centered within 0.3% to 7% from the expected position of full photonic bandgaps predicted by PWE (Fig. 4A). The observed deviations can be attributed to (i) the variability of geometric dimensions throughout the sample and (ii) the uncertainty of the refractive index measured by ellipsometry and used in PWE simulations. The SEM measurements and nested variance analysis showed ~1% in-plane (Table S1) and ~5% out-of-plane (Fig. S2) deviations of the lateral period throughout the woodpile, and the measured refractive index of a TiO_2 film of 2.3 is 4-15% lower than the expected index of 2.40-2.71 for rutile TiO_2 within a 1500-3000 nm range[29]. This could be caused by some inherent porosity in the TiO_2 film (Fig. S5, left) used for ellipsometry measurements; the

beams that comprise TiO_2 PhCs are fully dense. Uncertainty in the geometrical dimensions of up to 5% and in the refractive index of up to 15% can contribute to the observed deviations between experimental and simulated peak positions.

In summary, we developed an additive manufacturing process to create 3D nano-architected titania with a sub-micron resolution. We demonstrate the feasibility and efficiency of this process using a woodpile FCT architecture with individual feature widths of 150 nm as a model system. The as-fabricated material is carbon-free and consists homogeneous, fully dense nanoscrystalline rutile TiO_2. Taking advantage of the high refractive index and transparency of titania, we prototyped several PhCs with sub-micron lateral periods and full photonic bandgaps centered at 1.8-2.9 μm, consistently confirmed by PWE simulations and FTIR measurements. Fabricating PhCs with full photonic bandgaps in the visible requires lateral periods of ~300 nm[10], which can be achieved by modulating precursor loading. We showed that using lower concentrations of TiO_2 precursor allows for two times smaller features due to higher post-pyrolysis linear shrinkage. The developed freeform AM process is not limited to woodpile geometries and can be applied to directly fabricate a broad range of 3D architectures. This nano-scale AM process is also not limited to TiO_2: other hybrid organic-inorganic-based photopolymers can be formulated to print a variety of materials, including other dielectrics, metals, and semiconductors. AM of 3D nano-architected titania is poised to enable facile fabrication of components for a much broader set of applications, including micro-optics, 3D MEMS, and minimally invasive tools and procedures.

Supporting Information

Supporting information is available online and includes Materials and Methods, voxel shape modeling, additional figures and tables.

Figure captions

Figure 1. Process for nanoscale additive manufacturing (AM) of titanium dioxide and SEM characterization of as-fabricated TiO_2 3D architectures. (A) Ligand exchange reaction between titanium (IV) ethoxide and acrylic acid is used to synthesize a liquid TiO_2 precursor in the photopolymer. (B) Titania pre-ceramic photopolymer is used in a two-photon lithography process to fabricate pre-ceramic 3D architectures. (C) Schematic of a pre-ceramic woodpile architecture supported by a set of springs that decouple it from the substrate. (D) Titania woodpile structure is formed by calcination of the pre-ceramic part. (E,G) Representative SEM images of pre-ceramic woodpile architectures. (F, H, I) Representative TiO_2 woodpile architectures after calcination at 750-900°C. Scale bars are 50 μm for (E), 20 μm for (F), 2 μm for (G), 1 μm for (H), and 2 μm for (I)

Figure 2. Characterization of chemical composition and phase of TiO_2 using SEM EDS and Raman spectroscopy. (A-D) SEM EDS mapping of a representative woodpile architecture fabricated on a silicon substrate reveals uniform distribution of titanium and oxygen. (E) Estimation of chemical composition from a representative EDS spectrum shows 1:2 at% ratio of titanium to oxygen consistent with TiO_2. (F) Raman spectrum of as-fabricated TiO_2 compared to reference spectra of rutile and anatase. Scale bars are 50 μm for (A-D)

Figure 3. TEM characterization of as-fabricated TiO_2 3D architectures. (A) Low-magnification TEM image showing a 100 nm thick cross-section of a TiO_2 woodpile structure prepared using FIB lift-out procedure. (B) HRTEM image of a cross-section of an individual beam, an electron diffraction pattern (inset), and (C) a corresponding dark-field TEM image reveal that the beams consist predominantly out of nanocrystalline rutile TiO_2. (D) Grain size histogram for n=100 particles measured from an SEM image showing 95% confidence intervals on the mean grain size (μ) and the standard deviation (σ). Scale bars are 2 μm for (A), 5 nm for (B, C), and 2 nm^{-1} for (B, inset).

Figure 4. Optical characterization of 3D photonic crystals fabricated using the developed nanoscale AM process (A) Calculated band structure of the fabricated woodpile FCT architecture. Grey band shows the position of a full photonic band gap. (B) FTIR reflectance and transmittance spectra taken from a woodpile structure showing the emergence of high reflectance and low transmittance bands centered at 2.9 μm. (C) Schematic of a woodpile unit cell and SEM of representative woodpile structures with 1120 nm, 1030 nm, and 840 nm lateral periods fabricated using the developed AM method. (D) FTIR reflectance spectra for as-fabricated woodpile structures with varying periodicities showing passive tuning of the reflectance band position between 1.8 and 2.4 μm. Scale bars are 1 μm for (C).

Acknowledgements

The authors are grateful for the support of JRG's DoD Vannevar-Bush Faculty Fellowship. Authors also acknowledge AV's Resnick Sustainability Institute at Caltech Fellowship and NIH Biotechnology Leadership Pre-Doctoral Training Program support. We thank Professor George R. Rossman (Caltech) for his assistance with Raman spectroscopy and FTIR.

References

(1) Zocca, A.; Colombo, P.; Gomes, C. M.; Günster, J. Additive Manufacturing of Ceramics: Issues, Potentialities, and Opportunities. *J. Am. Ceram. Soc.* **2015**, *98* (7), 1983–2001.

(2) Melchels, F. P. W.; Domingos, M. A. N.; Klein, T. J.; Malda, J.; Bartolo, P. J.; Hutmacher, D. W. Additive Manufacturing of Tissues and Organs. *Prog. Polym. Sci.* **2012**, *37* (8), 1079–1104. https://doi.org/https://doi.org/10.1016/j.progpolymsci.2011.11.007.

(3) Frazier, W. E. Metal Additive Manufacturing: A Review. *J. Mater. Eng. Perform.* **2014**, *23* (6), 1917–1928. https://doi.org/10.1007/s11665-014-0958-z.

(4) Hirt, L.; Reiser, A.; Spolenak, R.; Zambelli, T. Additive Manufacturing of Metal Structures at the Micrometer Scale. *Adv. Mater.* **2017**, 1604211-n/a. https://doi.org/10.1002/adma.201604211.

(5) Vaezi, M.; Seitz, H.; Yang, S. A Review on 3D Micro-Additive Manufacturing Technologies. *Int. J. Adv. Manuf. Technol.* **2013**, *67* (5), 1721–1754. https://doi.org/10.1007/s00170-012-4605-2.

(6) Pikul, J. H.; Gang Zhang, H.; Cho, J.; Braun, P. V; King, W. P. High-Power Lithium Ion Microbatteries from Interdigitated Three-Dimensional Bicontinuous Nanoporous Electrodes. *Nat. Commun.* **2013**, *4*, 1732.

(7) Nelson, B. J.; Kaliakatsos, I. K.; Abbott, J. J. Microrobots for Minimally Invasive

Medicine. *Annu. Rev. Biomed. Eng.* **2010**, *12* (1), 55–85. https://doi.org/10.1146/annurev-bioeng-010510-103409.

(8) Yee, D. W.; Lifson, M. L.; Edwards, B. W.; Greer, J. R. Additive Manufacturing of 3D-Architected Multifunctional Metal Oxides. *Adv. Mater.* **2019**, *1901345*, 1–9. https://doi.org/10.1002/adma.201901345.

(9) Wong, S.; Deubel, M.; Pérez-Willard, F.; John, S.; Ozin, G. A.; Wegener, M.; Von Freymann, G. Direct Laser Writing of Three-Dimensional Photonic Crystals with a Complete Photonic Bandgap in Chalcogenide Glasses. *Adv. Mater.* **2006**, *18* (3), 265–269. https://doi.org/10.1002/adma.200501973.

(10) Frölich, A.; Fischer, J.; Zebrowski, T.; Busch, K.; Wegener, M. Titania Woodpiles with Complete Three-Dimensional Photonic Bandgaps in the Visible. *Adv. Mater.* **2013**, *25* (26), 3588–3592. https://doi.org/10.1002/adma.201300896.

(11) Camposeo, A.; Persano, L.; Farsari, M.; Pisignano, D. Additive Manufacturing: Applications and Directions in Photonics and Optoelectronics. *Adv. Opt. Mater.* **2019**, *7* (1). https://doi.org/10.1002/adom.201800419.

(12) Liu, J.; Ueda, M. High Refractive Index Polymers: Fundamental Research and Practical Applications. *J. Mater. Chem.* **2009**, *19* (47), 8907. https://doi.org/10.1039/b909690f.

(13) Haas, K. H.; Wolter, H. Synthesis, Properties and Applications of Inorganic-Organic Copolymers (ORMOCER®s). *Curr. Opin. Solid State Mater. Sci.* **1999**, *4* (6), 571–580. https://doi.org/10.1016/S1359-0286(00)00009-7.

(14) Jonušauskas, L.; Gailevičius, D.; Mikoliunaite, L.; Sakalauskas, D.; Šakirzanovas, S.; Juodkazis, S.; Malinauskas, M. Optically Clear and Resilient Free-Form μ-Optics 3D-Printed via Ultrafast Laser Lithography. *Materials (Basel).* **2017**, *10* (1), 1–18. https://doi.org/10.3390/ma10010012.

(15) Yeh, C. C.; Liu, H. C.; Heni, W.; Berling, D.; Zan, H. W.; Soppera, O. Chemical and Structural Investigation of Zinc-Oxo Cluster Photoresists for DUV Lithography. *J. Mater. Chem. C* **2017**. https://doi.org/10.1039/C6TC05201K.

(16) Malinauskas, M.; Ukauskas, A.; Purlys, V.; Gaidukeviiut, A.; Baleviius, Z.; Piskarskas, A.; Fotakis, C.; Pissadakis, S.; Gray, D.; Gadonas, R.; et al. 3D Microoptical Elements Formed in a Photostructurable Germanium Silicate by Direct Laser Writing. *Opt. Lasers Eng.* **2012**, *50* (12), 1785–1788. https://doi.org/10.1016/j.optlaseng.2012.07.001.

(17) Bond, W. L. Measurement of the Refractive Indices of Several Crystals. *J. Appl. Phys.* **1965**, *36* (5), 1674–1677. https://doi.org/10.1063/1.1703106.

(18) Passinger, S.; Saifullah, M. S. M.; Reinhardt, C.; Subramanian, K. R. V; Chichkov, B. N.; Welland, M. E. Direct 3D Patterning of TiO2 Using Femtosecond Laser Pulses. *Adv. Mater.* **2007**, *19* (9), 1218–1221. https://doi.org/10.1002/adma.200602264.

(19) Vyatskikh, A.; Delalande, S.; Kudo, A.; Zhang, X.; Portela, C. M.; Greer, J. R. Additive Manufacturing of 3D Nano-Architected Metals. *Nat. Commun.* **2018**, *9* (1), 593. https://doi.org/10.1038/s41467-018-03071-9.

(20) John, S. Strong Localization of Photons in Certain Disordered Dielectric Superlattices. *Phys. Rev. Lett.* **1987**, *58* (23), 2486–2489. https://doi.org/10.1103/PhysRevLett.58.2486.

(21) Yablonovitch, E. Inhibited Spontaneous Emission in Solid-State Physics and Electronics. *Phys. Rev. Lett.* **1987**, *58* (20), 2059–2062. https://doi.org/10.1103/PhysRevLett.58.2059.

(22) Susumu Noda; Katsuhiro Tomoda; Noritsugu Yamamoto; Alongkarn Chutinan. Full Three-Dimensional Photonic Bandgap Crystals at Near-Infrared Wavelengths. *Science (80-.).* **2000**, *289* (5479), 604–606. https://doi.org/10.1126/science.289.5479.604.

(23) Staude, I.; Thiel, M.; Essig, S.; Wolff, C.; Busch, K.; von Freymann, G.; Wegener, M. Fabrication and Characterization of Silicon Woodpile Photonic Crystals with a Complete Bandgap at Telecom Wavelengths. *Opt. Lett.* **2010**, *35* (7), 1094–1096. https://doi.org/10.1364/OL.35.001094.

(24) Von Freymann, G.; Ledermann, A.; Thiel, M.; Staude, I.; Essig, S.; Busch, K.; Wegener, M. Three-Dimensional Nanostructures for Photonics. *Adv. Funct. Mater.* **2010**, *20* (7), 1038–1052. https://doi.org/10.1002/adfm.200901838.

(25) Luo, C.; Johnson, S. G.; Joannopoulos, J. D. All-Angle Negative Refraction in a Three-Dimensionally Periodic Photonic Crystal. *Appl. Phys. Lett.* **2002**, *81* (13), 2352–2354. https://doi.org/10.1063/1.1508807.

(26) Ho, K. M.; Chan, C. T.; Soukoulis, C. M.; Biswas, R.; Sigalas, M. Photonic Band Gaps in Three Dimensions: New Layer-by-Layer Periodic Structures. *Solid State Commun.* **1994**, *89* (5), 413–416. https://doi.org/10.1016/0038-1098(94)90202-X.

(27) Chernow, V. F.; Ng, R. C.; Greer, J. R. Designing Core-Shell 3D Photonic Crystal Lattices for Negative Refraction. *Proc. SPIE* **2017**, *10112*. https://doi.org/10.1117/12.2251545.

(28) Aoki, K.; Guimard, D.; Nishioka, M.; Nomura, M.; Iwamoto, S.; Arakawa, Y. Coupling of Quantum-Dot Light Emission with a Three-Dimensional Photonic-Crystal Nanocavity. *Nat. Photonics* **2008**, *2* (11), 688–692. https://doi.org/10.1038/nphoton.2008.202.

(29) Ribarsky, M. W. - Titanium Dioxide (TiO2) (Rutile); Palik, E. D. B. T.-H. of O. C. of S., Ed.; Academic Press: Burlington, 1997; pp 795–804. https://doi.org/https://doi.org/10.1016/B978-012544415-6.50042-X.

(30) Duoss, E. B.; Twardowski, M.; Lewis, J. A. Sol-Gel Inks for Direct-Write Assembly of Functional Oxides. *Adv. Mater.* **2007**, *19* (21), 3485–3489. https://doi.org/10.1002/adma.200701372.

(31) Yu, S.-Y.; Schrodj, G.; Mougin, K.; Dentzer, J.; Malval, J.-P.; Zan, H.-W.; Soppera, O.; Spangenberg, A. Direct Laser Writing of Crystallized TiO2 and TiO2/Carbon Microstructures with Tunable Conductive Properties. *Adv. Mater.* **2018**, *30* (51), 1805093. https://doi.org/10.1002/adma.201805093.

(32) Vyatskikh, A.; Kudo, A.; Delalande, S.; Greer, J. R. Additive Manufacturing of Polymer-Derived Titania for One-Step Solar Water Purification. *Mater. Today Commun.* **2018**, *15* (March), 288–293. https://doi.org/10.1016/j.mtcomm.2018.02.010.

(33) Vyatskikh, A.; Ng, R. C.; Edwards, B.; Greer, J. R. Additive Manufacturing of Titanium Dioxide for Dielectric Photonic Crystals. In *Proc.SPIE*; 2019; Vol. 10930.

(34) Sun, H. B.; Tanaka, T.; Kawata, S. Three-Dimensional Focal Spots Related to Two-Photon Excitation. *Appl. Phys. Lett.* **2002**, *80* (20), 3673–3675. https://doi.org/10.1063/1.1478128.

(35) Serbin, J.; Egbert, A.; Ostendorf, A.; Chichkov, B. N.; Houbertz, R.; Domann, G.; Schulz, J.; Cronauer, C.; Fröhlich, L.; Popall, M. Femtosecond Laser-Induced Two-Photon Polymerization of Inorganic–Organic Hybrid Materials for Applications in Photonics. *Opt. Lett.* **2003**, *28* (5), 301. https://doi.org/10.1364/OL.28.000301.

(36) Uppal, N. Modeling of Temperature-Dependent Diffusion and Polymerization Kinetics and Their Effects on Two-Photon Polymerization Dynamics. *J. Micro/Nanolithography, MEMS, MOEMS* **2008**. https://doi.org/10.1117/1.3033203.

(37) Montgomery, D. C. *Design and Analysis of Experiments*; John Wiley & Sons, Inc.: USA, 2006.

(38) Leonard, D. N.; Chandler, G. W.; Seraphin, S. Scanning Electron Microscopy. In *Characterization of Materials*; John Wiley & Sons, Inc., 2002. https://doi.org/10.1002/0471266965.com081.pub2.

(39) Frank, O.; Zukalova, M.; Laskova, B.; Kürti, J.; Koltai, J.; Kavan, L. Raman Spectra of Titanium Dioxide (Anatase, Rutile) with Identified Oxygen Isotopes (16, 17, 18). *Phys. Chem. Chem. Phys.* **2012**, *14* (42), 14567–14572. https://doi.org/10.1039/c2cp42763j.

(40) Ding, X. Z.; Qi, Z. A.; He, Y. Z. Effect of Tin Dioxide Doping on Rutile Phase Formation in Sol-Gel-Derived Nanocrystalline Titania Powders. *Nanostructured Mater.* **1994**, *4* (6), 663–668. https://doi.org/10.1016/0965-9773(94)90018-3.

(41) Mueller, J. B.; Fischer, J.; Mayer, F.; Kadic, M.; Wegener, M. Polymerization Kinetics in Three-Dimensional Direct Laser Writing. *Adv. Mater.* **2014**, *26* (38), 6566–6571. https://doi.org/10.1002/adma.201402366.

(42) Mueller, J. B.; Fischer, J.; Mange, Y. J.; Nann, T.; Wegener, M. In-Situ Local Temperature Measurement during Three-Dimensional Direct Laser Writing. *Appl. Phys. Lett.* **2013**, *103* (12). https://doi.org/10.1063/1.4821556.

(43) Forouhi, A. R.; Bloomer, I. Optical Dispersion Relations for Amorphous Semiconductors and Amorphous Dielectrics. *Phys. Rev. B* **1986**, *34* (10), 7018–7026. https://doi.org/10.1103/PhysRevB.34.7018.

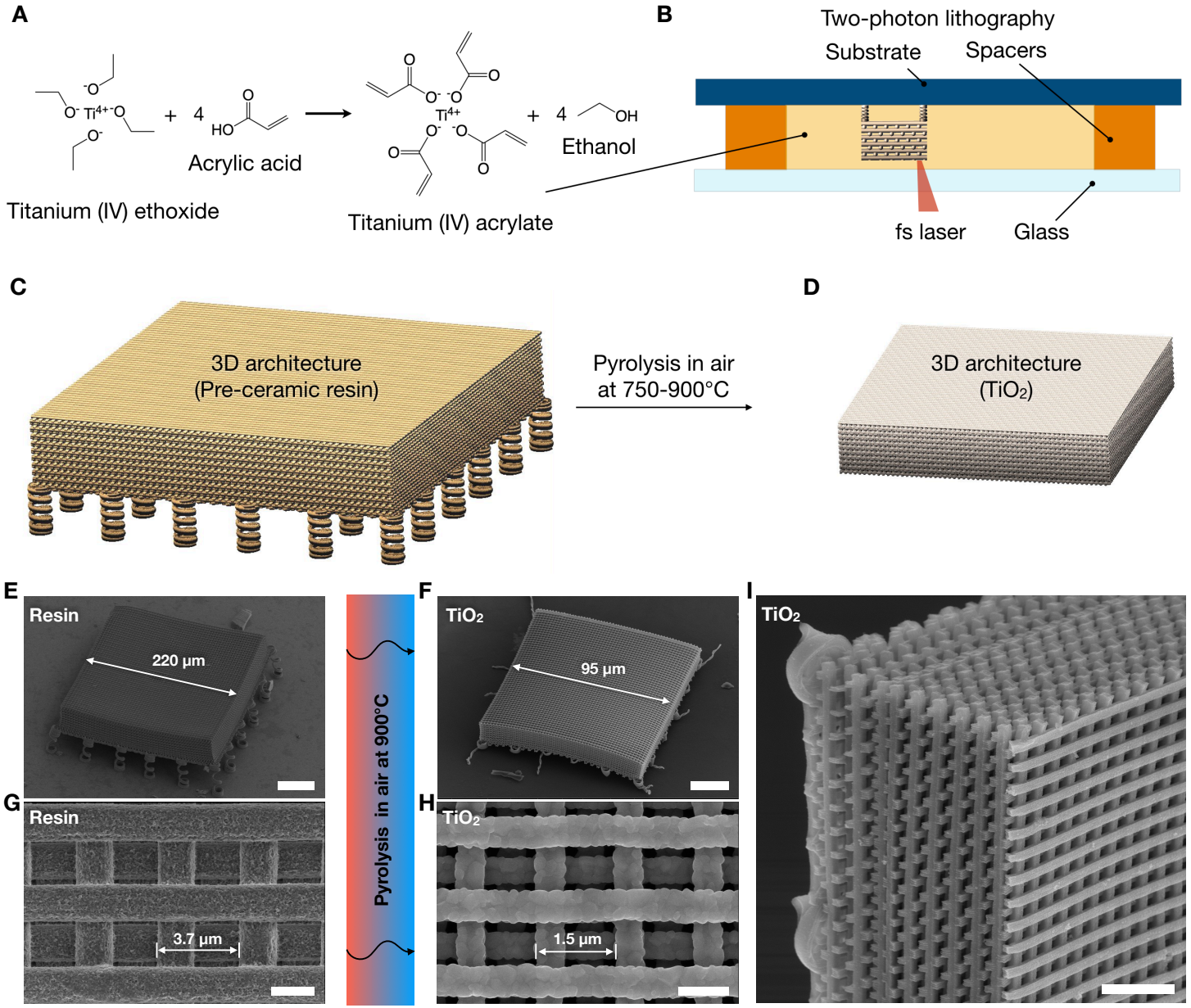
A
Titanium (IV) ethoxide
Acrylic acid
Titanium (IV) acrylate
Ethanol
B
Two-photon lithography
Substrate
Spacers
fs laser
Glass
C
3D architecture
(Pre-ceramic resin)
Pyrolysis in air
at 750-900°C
D
3D architecture
(TiO2)
E
Resin
220 µm
G
Resin
3.7 µm
Pyrolysis in air at 900°C
F
TiO2
95 µm
H
TiO2
1.5 µm
I
TiO2

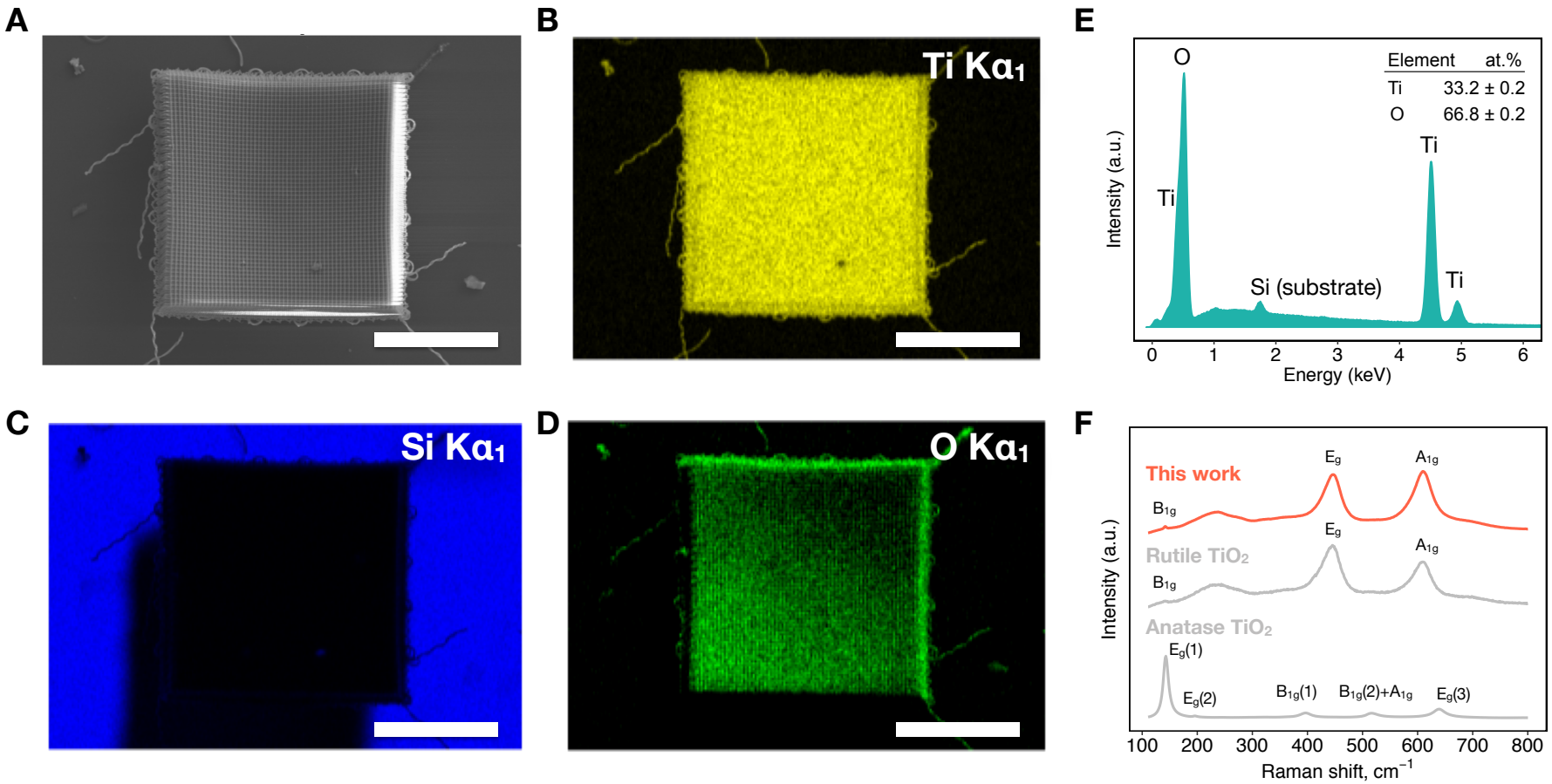
A
B
Ti Kα1
C
Si Kα1
D
O Kα1
E
O
Ti
Ti
Si (substrate)
Ti
Element at.%
Ti 33.2 ± 0.2
O 66.8 ± 0.2
Intensity (a.u.)
Energy (keV)
F
This work
Rutile TiO2
Anatase TiO2
Eg
A1g
B1g
Eg(1)
Eg(2)
B1g(1)
B1g(2)+A1g
Eg(3)
Intensity (a.u.)
Raman shift, cm−1

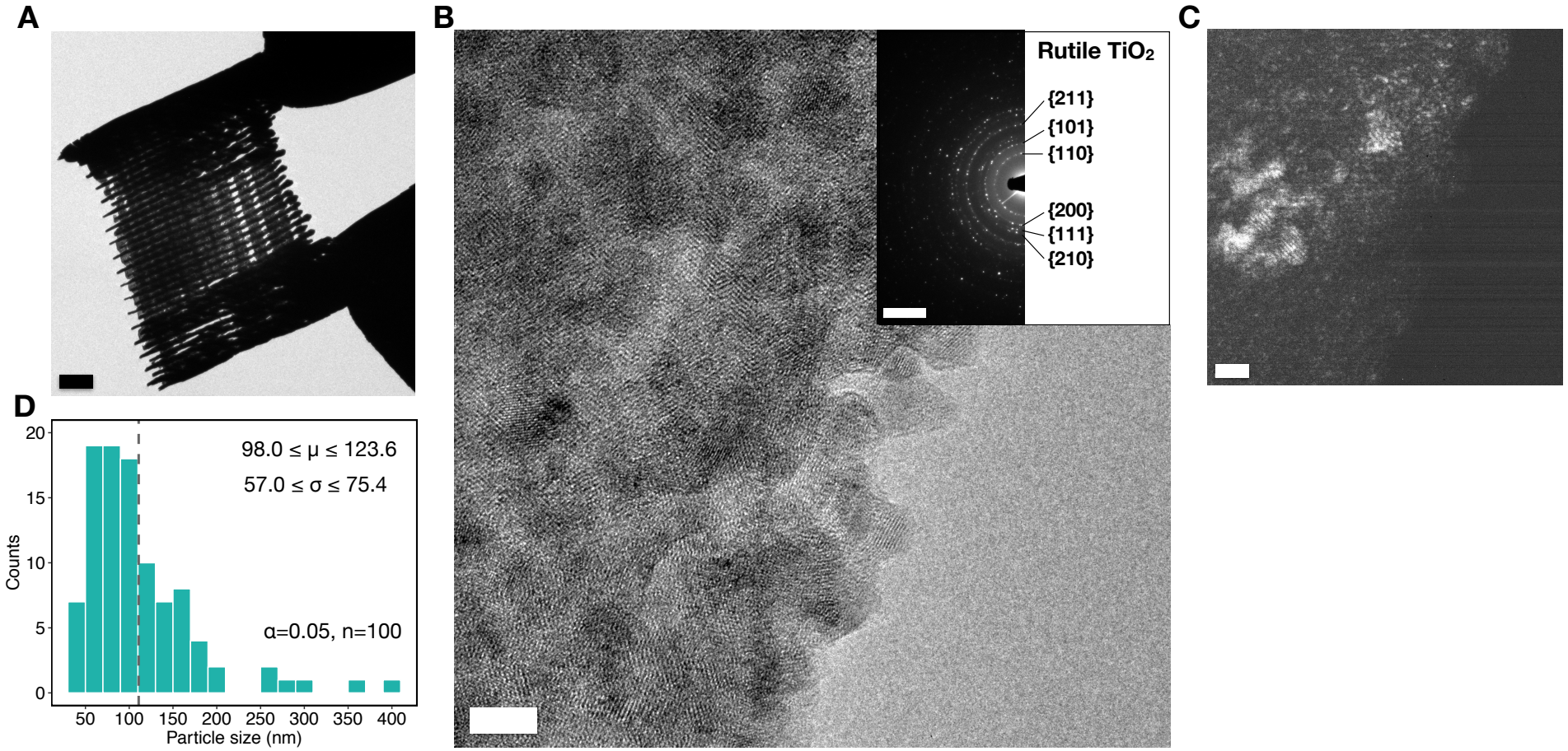
A
B
C
D
Rutile TiO2
{211}
{101}
{110}
{200}
{111}
{210}
98.0 ≤ μ ≤ 123.6
57.0 ≤ σ ≤ 75.4
α=0.05, n=100
Counts
Particle size (nm)

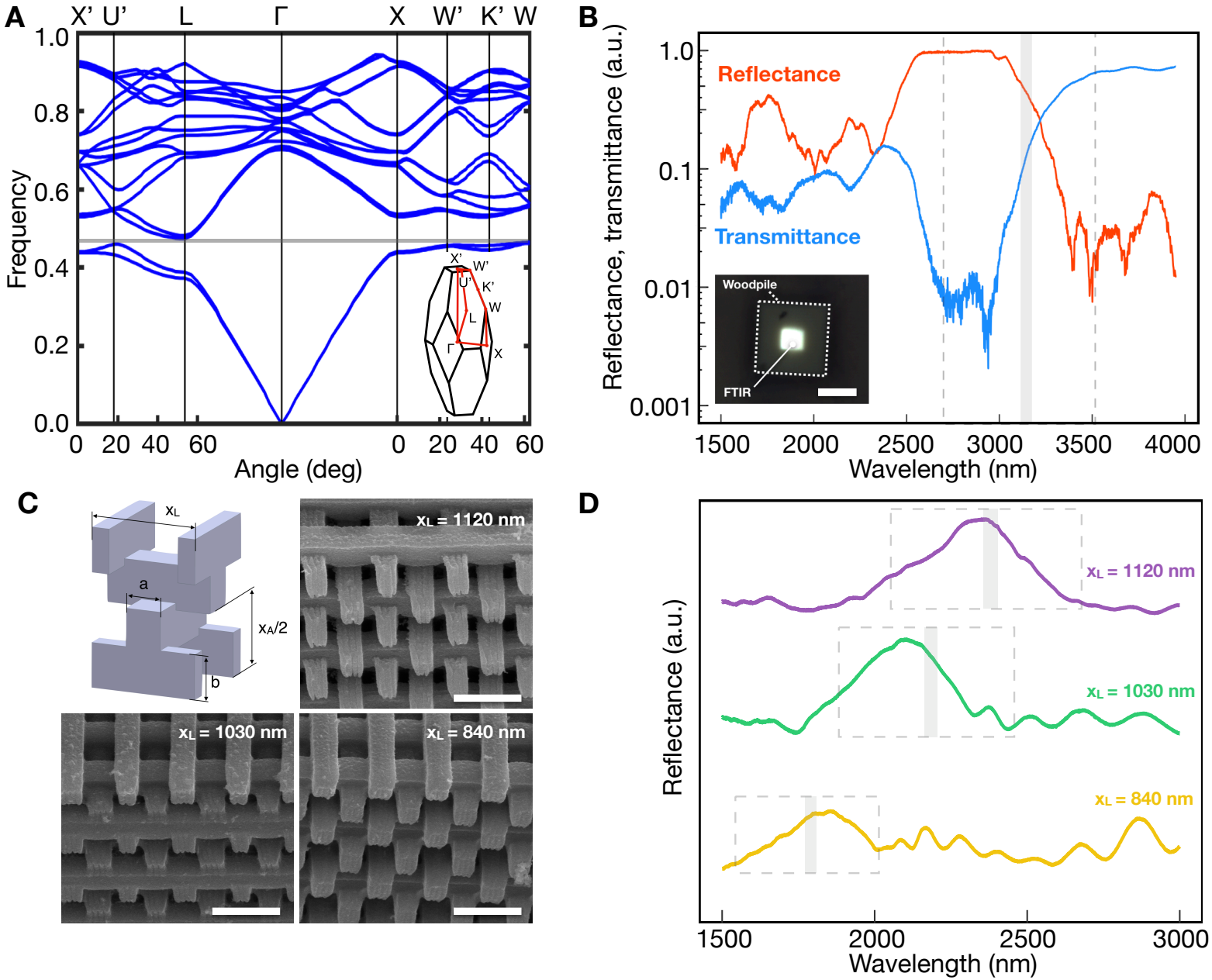
A
X' U' L Γ X W' K' W
Frequency
Angle (deg)
B
Reflectance
Transmittance
Reflectance, transmittance (a.u.)
Wavelength (nm)
Woodpile
FTIR
C
xL
a
xA/2
b
xL = 1120 nm
xL = 1030 nm
xL = 840 nm
D
Reflectance (a.u.)
Wavelength (nm)